Journal of Energy Storage 141 (2026) 119206

Contents lists available at ScienceDirect

Journal of Energy Storage

journal homepage: www.elsevier.com/locate/est

Research papers

A 3D battery model incorporating Si particle expansion induced electrolyte motion

Lioba Boveleth [a,b], Max Okraschevski [a,b], Timo Danner [a,b,*], Arnulf Latz [a,b,c]

[a] German Aerospace Center, Institute of Engineering Thermodynamics, Pfaffenwaldring 38-40, Stuttgart, 70569, Germany
[b] Helmholtz Institute Ulm for Electrochemical Energy Storage, Helmholtzstraße 11, Ulm, 89081, Germany
[c] Ulm University, Institute of Electrochemistry, Albert-Einstein-Allee 47, Ulm, 89081, Germany

ARTICLE INFO

Keywords:
Lithium-ion battery
Silicon-graphite
Large volume expansion
Electrolyte flow
Volume-averaged model
Discontinuous Galerkin

ABSTRACT

Silicon is frequently used as active material in the negative electrode of Lithium-ion batteries as it provides substantial improvements in the energy density compared to conventional graphite electrodes. Due to large volume changes during cycling, the Si content in state-of-the-art Si/graphite composite electrodes is often rather low. As significantly higher Si contents are desirable, the effects of structural changes that influence ion and electron transport and, thus, battery performance and degradation have to be analyzed. An aspect which is often overlooked is the displacement of electrolyte into the void regions of the cells.

In our work, we developed a homogenized electrochemical model of Li-ion batteries including single phase flow through the porous electrode media to account for electrolyte motion. The considered Darcy flow is generated by the change in active material volume during battery operation. In our studies, we keep track of the amount of displaced electrolyte and the Li concentration therein. Considering different material compositions and cell designs highlights that the ratio of anode and cathode thickness and permeability are the dominant parameters determining the Li concentration in the displaced electrolyte volume.

The difference between inner and displaced electrolyte Li concentration results in a concentration gradient in outflow direction. While the accumulation or depletion of local Li concentration favors degradation during prolonged cycling, our simulations show that this effect can be mitigated by tuning the permeability.

1. Introduction

The improvement of Lithium-ion (Li-ion) batteries plays a key role to meet the targets of the automotive sector. A promising material for the negative electrode is silicon (Si), which is both abundant and offers a ten times higher theoretical capacity (3579 mAh/g for $Li_{15}Si_4$) compared to graphite (372 mAh/g for LiC_6) [1]. However, large volume changes during lithiation and delithiation and general low Li mobility compromise the cycle life of Si anodes [2,3]. Thus, applications focus on Si/graphite composite anodes [4,5]. Mechanistic insights on electrochemical mechanisms and their effect on structural changes, specifically porosity changes, of Si/graphite anodes are given by Vidal et al. [6]. In their study, they report the well-known competition between (de-)lithiation of Si and graphite in composite anodes. Moreover, they observe an asymmetry in the swelling behavior during charge and discharge as Si is lithiated simultaneously with graphite but delithiated after graphite. The exact contribution during lithiation depends on the applied C-rate [7], as well as material parameters [8]. Several studies investigate the impact of increasing Si fractions on cell properties [9–11].

While the internal stresses resulting from volume changes have been studied intensively [12–15], the electrolyte motion in battery cells was measured just recently [16]. Follow up publications provide quantitative measurements of displaced electrolyte volume and visual confirmation and quantification of displaced electrolyte volume using operando synchrotron tomography [17,18]. The latter study also highlights the impact of different cell designs and orientation. These kind of effects have to be studied in three dimensions (3D) to realistically simulate flow conditions. Several groups started adding electrolyte displacement to their battery models [3,19–21]. Yu et al. [3] developed a pseudo-three-dimensional (p3D) electrochemo-mechanical coupled model that accounts for electrolyte flow induced by pore pressure gradients. Their insights into the mutual influences of electrolyte flow and the stress, temperature or electrochemical field, however, suggest negligible impact of electrolyte flow. This result is mainly due to their choice of active materials and boundary conditions and limiting their model to the cells discharge without analyzing the impact of the electrolyte leakage in further battery operation. Kulathu et al. [19] extended the

* Corresponding author at: German Aerospace Center, Institute of Engineering Thermodynamics, Pfaffenwaldring 38-40, Stuttgart, 70569, Germany.
E-mail address: timo.danner@dlr.de (T. Danner).

https://doi.org/10.1016/j.est.2025.119206
Received 6 June 2025; Received in revised form 14 September 2025; Accepted 26 October 2025
Available online 1 November 2025

model formulation and implemented a p4D framework for virtual cell design. They demonstrate significantly higher flow velocities, however did not analyze in detail the influence of displaced electrolyte on salt concentration. The p2D formulation of Hamedi et al. [21] includes the large local volume changes of Si and the resulting stress effects. The authors investigate the impact of Si content and cell housing on expansion and electrochemical properties. Due to the 1D transport formulation, electrolyte flow to a reservoir is using source terms and the reservoir and its concentration are not specifically resolved. Combining several experimental methods and simulations, Solchenbach et al. [20] investigate in detail electrolyte motion and its impact on cell cycling. In their p3D model, electrolyte displacement in the void volume within the cell results in in-plane $LiPF_6$ concentration gradients, called electrolyte motion induced salt inhomogeneity (EMSI), which cause highly localized Li plating. As outlined in previous works, this Li plating leads to rapid degradation and fundamental safety risks [8,22].

Following up the work of Solchenbach et al. [20], we use an extended simulation approach to study electrolyte motion in Si/graphite composite anodes with increasing Si content. In particular, we additionally consider lithiation in Si and graphite as well as their expansion separately. The resulting convection and exchange with the reservoir are studied in all domains. Furthermore, the extension to 3D enables the analysis of the impact of different outflow regions and boundary conditions. This is of particular practical relevance enabling engineering of cell design. The model is implemented in the open-source tool Firedrake providing an efficient, high-level numerical framework for battery simulations [23].

In our simulations, we analyze the impact of varying Si contents in Si/graphite anodes considering full-cells with an NMC cathode. Our model allows to track electrolyte flow and resulting Li concentration within the electrolyte that was pushed out of the electrodes and separator. Variations of permeability, cell size, boundary, and operation conditions help to understand their impact on electrolyte motion and salt inhomogeneities. The insights of our study provide guidelines for the optimization of Si composite electrodes. In particular, we are able to show that optimization of electrode and component permeability might be a strategy to mitigate inhomogeneous salt distribution and resulting degradation effects.

2. Methods

This section describes the derivation and realization of our battery cell model. The resulting Si/graphite-NMC622 full-cells are schematically illustrated in Fig. 1. The electrodes are modeled as homogeneous porous media consisting of solid particles. The pore space is completely wetted with incompressible liquid electrolyte. Together with the porous and fully wetted separator they form the simulation domain Ω. In case of a cylindrical cell, we simulate a 2D domain illustrated in Fig. 1 (a). The cylindrical cell itself has a constant volume with a rigid casing and void regions at the top and the bottom due to connectors and electrode overhang. While those are initially filled with excess electrolyte (V_e^{Free}), the amount of electrolyte therein varies during battery operation as observed in [20]. Note that the height of the cells (about 10 cm) is significantly larger compared to the cell thickness (about 100 µm) consisting of current collectors, anode, separator, and cathode. In our study, we use the height in [20] as the 4695 cell format is becoming increasingly popular. The y-direction is orthogonal to both the charge transport and flow directions. Since no transport is assumed in this direction, it is homogeneous and not resolved.

Furthermore, we consider also a prismatic cell format which has a blade-like shape [24–26] with a height of 90.3 and a width of 8.25 cm [26]. Fig. 1 (b) shows a representative 3D simulation domain of those large format cells. On all sides, the boundary conditions can be chosen to allow or prevent electrolyte flow. By modeling electrolyte flow only at the top and bottom of the domain, conditions of wound up prismatic cells are mimicked. In a stacked prismatic cell, void regions enabling electrolyte outflow are found on the left and the right, additionally.

The domain Ω comprises the electrochemically active region, exclusively consisting of solid and liquid phases. In contrast to the cathode, the anode consists of two active materials, Si and graphite. We account for each active material individually. In the following, subscripts indicate solid (s) or electrolyte (e) and initial (0) or maximum (max) values, while superscripts denote the active materials (mat ∈ {Si, Gr, NMC}).

To avoid the full resolution of the phases on microscale and the associated structural changes, we apply porous electrode theory and perform a change of scale by the method of volume averaging based on the work of Whitaker [27]. Structural changes, namely the temporal evolution of volume fractions of the solid and liquid phases, are derived by Schmitt et al. [28]. For our two-phase system, the averaging volume is expressed as $\mathcal{V} = V_e + V_s$, such that the porosity is given as

$$\varepsilon = \frac{V_e}{\mathcal{V}}. \tag{1}$$

The porosity of the electrodes is determined by the volume fractions of the respective active materials, namely $\varepsilon = 1-\varepsilon_s^{\text{Si}}-\varepsilon_s^{\text{Gr}}$ and $\varepsilon = 1-\varepsilon_s^{\text{NMC}}$, in anode and cathode, respectively. Note that porosity is in this case the natural parameter to describe the porous media, compared to other common descriptors like packing density. Changes in porosity (see Eq. (7)), equivalent to changes in electrolyte volume, drive the electrolyte displacement and therefore determine the convection velocity (see Eq. (19)). The porosity in the separator is constant. The superficial average of any quantity ζ is defined by

$$\langle \zeta_i \rangle = \frac{1}{\mathcal{V}} \int_{V_i} \zeta_i dV \tag{2}$$

and the material average by

$$\bar{\zeta}_i = \frac{1}{V_i} \int_{V_i} \zeta_i dV, \tag{3}$$

which are related according to $\langle \zeta_i \rangle = \varepsilon_i \bar{\zeta}_i$, $i \in \{e, s\}$. As the method of volume averaging is applied, the transport equations are integrated over a porous region and Gauss's theorem is used to derive the equations for the separate domains and the contribution of interfaces [27]. This porous region is small relative to the overall dimensions of the electrode but large relative to the pore structure [29].

2.1. Electrochemical model

A 3D microstructure-resolved model was presented in [30–32] and is summarized in the Supplementary Material. Volume averaging is applied to the model and, specifically aspects related to the active material expansion and contraction, will be elaborated hereinafter.

For the calculation of geometrical properties, we assume a homogeneous porous media consisting of spherical particles with radius R_p^{mat}. Thus, the specific surface area a^{mat} is given by the surface area of the respective particle divided by its volume which results in

$$a^{\text{mat}} = \frac{4\pi \left(R_p^{\text{mat}}\right)^2 \varepsilon_s^{\text{mat}}}{\frac{4}{3}\pi \left(R_p^{\text{mat}}\right)^3} = \frac{3\varepsilon_s^{\text{mat}}}{R_p^{\text{mat}}}. \tag{4}$$

The interface conditions are multiplied by a^{mat} when calculating the surface integral for the flux through all particle surfaces. Note that we do not add a further pseudo dimension to calculate the transport within a representative particle. Furthermore, the maximal Li concentration in the active materials is scaled to the current volume by

$$c_{s,max}^{\text{mat}} = c_{s,max_0}^{\text{mat}} \cdot \left(\frac{\varepsilon_s^{\text{mat}}}{\varepsilon_{s,0}^{\text{mat}}}\right)^{-1} \tag{5}$$

in order to calculate the Butler–Volmer flux with respect to the averaged concentrations. Finally, the effective diffusion and conductivity

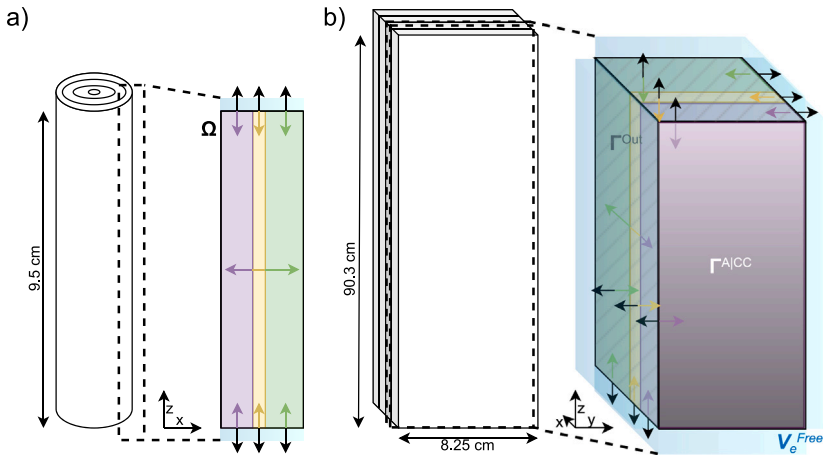

Fig. 1. Schematic of (a) a cylindrical cell and (b) a large format prismatic cell (blade-type design). The simulation domain Ω consists of anode (violet), separator (yellow), and cathode (green) and is connected to excess electrolyte V_e^{Free} (blue) at the outflow boundaries Γ^{Out}. At the remaining depicted boundaries are the anode and cathode current collectors ($A|CC$ and $C|CC$), respectively. (For interpretation of the references to color in this figure legend, the reader is referred to the web version of this article.)

constants of the liquid and solid phases are calculated based on the Bruggeman correlation, namely

$$\zeta_{i,\text{eff}} = \varepsilon_i \cdot \tau_i^{-1} \cdot \zeta_i \tag{6}$$

with $\zeta_i \in \{\kappa_i, D_i\}$, $i \in \{e, s\}$, and $\tau_i = \varepsilon_i^{-0.5}$.

2.2. Active material volume change

The change in porosity caused by (de-)lithiation induced volume change of the active materials is given by

$$\frac{\partial \varepsilon}{\partial t} = \sum_{\text{mat}} J^{\text{mat}} \hat{V}^{\text{mat}} \frac{V^{\text{mat}}}{c^{\text{mat}}_{s,max_0} V^{\text{mat}}_{max}} \tag{7}$$

with the Li source term J^{mat} taking the interface reaction including Eq. (4) and the solid phase diffusion into account [33]. V^{mat} describes the molar volume of the respective lithiated material and is expressed as a function of normalized Li concentration x_s^{mat} given by

$$x_s^{\text{mat}} = \frac{c_s^{\text{mat}}}{c^{\text{mat}}_{s,max}}. \tag{8}$$

$\hat{V}^{\text{mat}}$ is the partial derivative of the ratio of molar volumes according to

$$\hat{V}^{\text{mat}} = \frac{\partial \frac{V^{\text{mat}}}{V_0^{\text{mat}}}}{\partial x_s^{\text{mat}}}, \tag{9}$$

as we derive the volume change ratio next.

Alloying of Si. Obrovac et al. [34] derived a description for the volume of alloy materials. The linear expansion of Si during lithiation has been confirmed by in situ atomic force microscopy studies. Considering that a maximum of 3.75 Li atoms can be electrochemically added per Si atom at room temperature, Chandrasekaran et al. [1,35] express the molar volume of $\text{Li}_x\text{Si}_{4/15}$ as

$$V^{LiSi_{4/15}} = \frac{4}{15}\left(V_0^{\text{Si}} + 3.75 x_s^{\text{Si}} V^{\text{Li}}\right) \tag{10}$$

with the partial molar volume of Si, V_0^{Si}, and Li, V^{Li}. The fractional volume of lithiated Si follows as

$$\frac{V^{\text{Si}}}{V_0^{\text{Si}}}(x_s) = 1 + \frac{3.75 x_s^{\text{Si}} V^{\text{Li}}}{V_0^{Si}} \tag{11}$$

and for the radius

$$R_p^{\text{Si}} = R_{p_0}^{\text{Si}} \cdot \left(1 + \frac{3.75 x_s^{\text{Si}} V^{\text{Li}}}{V_0^{Si}}\right)^{\frac{1}{3}}. \tag{12}$$

Intercalation in graphite and NMC. Intercalation materials do not exhibit a linear volume change behavior. Hence, the following polynomial fit functions for the fractional volumes of graphite and NMC imaged in [36,37] and obtained with [38,39] are used:

$$\frac{V^{\text{Gr}}}{V_0^{\text{Gr}}}(x_s) = 2.69x_s^6 - 9.137x_s^5 + 11.29x_s^4 - 5.918x_s^3 + 1.057x_s^2 + 0.1207x_s + 1 \tag{13}$$

$$\frac{V^{\text{NMC}}}{V_0^{\text{NMC}}}(x_s) = 9.384x_s^6 - 31.92x_s^5 + 42.95x_s^4 - 28.67x_s^3 + 9.612x_s^2 - 1.345x_s + 1. \tag{14}$$

Accordingly, the respective particle radii are given by

$$R_p^{\text{mat}} = R_{p0}^{\text{mat}} \cdot \left(\frac{V^{\text{mat}}}{V_0^{\text{mat}}}\right)^{\frac{1}{3}}. \tag{15}$$

We approximate $V_0^{\text{Gr}} = 7.5 \cdot 10^{-6}$ m^3/mol and $V_0^{\text{NMC}} = 2 \cdot 10^{-6}$ m^3/mol [37] as well as $V^{\text{Li}} = 9 \cdot 10^{-6}$ m^3/mol and $V_0^{\text{Si}} = 12 \cdot 10^{-6}$ m^3/mol [1]. From (7), we obtain

$$\frac{\partial \varepsilon}{\partial t} = \left(\frac{a^{\text{Gr}} i^{\text{Gr}}}{F} - \nabla \cdot \left(D^{\text{Gr}}_{s,eff} \nabla c_s^{\text{Gr}}\right)\right) \hat{V}^{\text{Gr}} \frac{V^{\text{Gr}}}{c^{\text{Gr}}_{s,max_0} V^{\text{Gr}}_{max}} + \left(\frac{a^{\text{Si}} i^{\text{Si}}}{F} - \nabla \cdot \left(D^{\text{Si}}_{s,eff} \nabla c_s^{\text{Si}}\right)\right) \hat{V}^{\text{Si}} \frac{V^{\text{Si}}}{c^{\text{Si}}_{s,max_0} V^{\text{Si}}_{max}} \tag{16}$$

and

$$\frac{\partial \varepsilon}{\partial t} = \left(\frac{a^{\text{NMC}} i^{\text{NMC}}}{F} - \nabla \cdot \left(D^{\text{NMC}}_{s,eff} \nabla c_s^{\text{NMC}}\right)\right) \hat{V}^{\text{NMC}} \frac{V^{\text{NMC}}}{c^{\text{NMC}}_{s,max_0} V^{\text{NMC}}_{max}} \tag{17}$$

for anode and cathode, respectively, with current density i^{mat}. For the volume-averaged model, Eqs. (16) and (17) are calculated based on the averaged value $\bar{c}_s^{\text{mat}}$ using Eqs. (5) and (8), since the porosity ε and, correspondingly, the volume fractions $\varepsilon_s^{\text{mat}}$ are already in respect to the porous structure.

2.3. Flow model

The change in porosity caused by the volume change of the active materials induces electrolyte motion. The resulting advection within the domain and the amount of displaced electrolyte can be calculated by solving the mass and momentum balances for the velocity $\boldsymbol{v}$ and the pressure P. Assuming laminar flow for incompressible porous media, the Navier–Stokes equations simplify to

$$\nabla \cdot \boldsymbol{v} = 0 \qquad \text{and} \qquad 0 = -\nabla p + \nu \Delta \boldsymbol{v} \tag{18}$$

(low Reynold numbers $Re \ll 1$, high Schmidt numbers $Sc \gg 1$, and constant density ρ with dynamic pressure $p = P/\rho$). The kinematic viscosity is given by $\nu = \mu/\rho$ [40].

Volume averaging of the flow model yields

$$0 = \langle \nabla \cdot \boldsymbol{v} \rangle = \nabla \cdot \langle \boldsymbol{v} \rangle + \sum_{\text{mat}} \left(-\frac{\partial \epsilon_s^{\text{mat}}}{\partial t} \right), \tag{19}$$

$$\langle \boldsymbol{v} \rangle = -\frac{\boldsymbol{K}}{\mu} \nabla \bar{p}, \tag{20}$$

which will be combined to

$$0 = \nabla \cdot \left(-\frac{K}{\mu} \nabla \bar{p} \right) + \sum_{\text{mat}} \left(-\frac{\partial \epsilon_s^{\text{mat}}}{\partial t} \right). \tag{21}$$

In our model, we neglect density fluctuations due to variations in the electrolyte salt concentration since particle expansion is the dominating effect during operation. We apply the Carman–Kozeny equation for the permeability K [3,41] in the anode and cathode given by

$$K^{\text{Ano}} = \frac{\varepsilon^3 \left(\frac{2}{\epsilon_s^{\text{Gr}} + \epsilon_s^{\text{Si}}} \left(R_p^{\text{Gr}} \cdot \varepsilon_s^{\text{Gr}} + R_p^{\text{Si}} \cdot \varepsilon_s^{\text{Si}} \right) \right)^2}{C^{\text{Ano}} (1-\varepsilon)^2} \tag{22}$$

$$\text{and} \quad K^{\text{Cat}} = \frac{\varepsilon^3 \left(2R_p^{\text{NMC}} \right)^2}{C^{\text{Cat}} (1-\varepsilon)^2}, \tag{23}$$

respectively. The constants C^{Ano} and C^{Cat} are determined based on a given initial electrode structure. The pore size is smaller in the separator [42]. We assume

$$K^{Sep} = \frac{\varepsilon^3 \frac{2}{3} \left(2R_{p_0}^{\text{Si}} \right)^2}{C^{\text{Ano}} (1-\varepsilon)^2} = 1 \cdot 10^{-17}, \tag{24}$$

which is in the range of values provided in [43].

2.4. Overview of the model equations

An overview of the model equations in the simulation domain $\Omega = \Omega^{Cat} \cup \Omega^{Sep} \cup \Omega^{Ano}$ is provided in Table 1. Note that a convective term is included in the mass balance of the electrolyte. The set of equations allows to solve for the unknowns $\bar{p}$, ϵ_s^{Si}, ϵ_s^{Gr}, ϵ_s^{NMC}, $\bar{c}_s^{\text{Si}}$, $\bar{c}_s^{\text{Gr}}$, $\bar{c}_s^{\text{NMC}}$, $\bar{c}_e$, $\bar{\phi}_s^{\text{Ano}}$, $\bar{\phi}_s^{\text{Cat}}$, and $\bar{\varphi}_e$. The domain boundary Γ is split into the outflow boundary Γ^{Out}, the intersections to the current collectors $\Gamma^{A|CC}$ and $\Gamma^{C|CC}$, and the boundaries isolated for all unknowns Γ^N. Under the assumption of an adjoining reservoir and unrestrained electrolyte outflow, Dirichlet boundary conditions are applied at the outflow boundary. As those are gauge invariant, we set $p_D = 0$ N/m^2.

2.5. Electrolyte reservoir

The total amount of electrolyte V_e^{Total} is given by the sum of the electrolyte within the resolved domain V_e^{Ω} and the electrolyte pushed out of the domain V_e^{Free}, namely

$$V_e^{\text{Total}} = V_e^{\Omega} + V_e^{\text{Free}} \tag{25}$$

$$V_e^{\Omega} = \int_{\Omega} \varepsilon \, dx. \tag{26}$$

The displaced electrolyte is explicitly calculated after each time step k

$$V_{e,k}^{\text{Free}} = V_{e,k-1}^{\text{Free}} + (t_k - t_{k-1}) \cdot \int_{\Gamma^{Out}} \left(-\frac{K}{\mu} \right) \nabla \bar{p} \cdot \boldsymbol{n} \, ds. \tag{27}$$

Note that the flow direction depends on the direction of the pressure gradient. In contrast to [20,21], we take excess electrolyte into account and initialize $V_{e,0}^{\text{Free}}$ as 5 % of the initial electrolyte amount within Ω with $c_{e,0}^{\text{Free}} = \bar{c}_{e,0}$. Additionally, we track the amount of Li within V_e^{Free} according to

$$N_k^{Li,\text{Free},out} = N_{k-1}^{Li,\text{Free}} + (t_k - t_{k-1}) \cdot \int_{\Gamma^{Out}} \bar{c}_e \left(-\frac{K}{\mu} \right) \nabla \bar{p} \cdot \boldsymbol{n} ds \tag{28}$$

Table 1
Summary of equations used for full-cell charge simulations. Otherwise isolating Neumann conditions are applied for the respective unknowns.

	$-\kappa_{s,eff}^{\text{NMC}} \nabla \bar{\phi}_s^{\text{Cat}} \cdot \boldsymbol{n} = \frac{I_{\text{app}}}{A_{\text{cell}}}$ on $\Gamma^{C\|CC}$	
in Ω^{Cat}	$0 = \nabla \cdot \left(-\frac{K^{\text{Cat}}}{\mu} \nabla \bar{p} \right) + \left(\frac{a^{\text{NMC}} i^{\text{NMC}}}{F} - \nabla \cdot \left(D_{s,eff}^{\text{NMC}} \nabla \bar{c}_s^{\text{NMC}} \right) \right) \hat{V}^{\text{NMC}} \frac{V^{\text{NMC}}}{c_{s,max_0}^{\text{NMC}} V_{max}^{\text{NMC}}}$	
	$0 = \frac{\partial \epsilon_s^{\text{NMC}}}{\partial t} + \left(\frac{a^{\text{NMC}} i^{\text{NMC}}}{F} - \nabla \cdot \left(D_{s,eff}^{\text{NMC}} \nabla \bar{c}_s^{\text{NMC}} \right) \right) \hat{V}^{\text{NMC}} \frac{V^{\text{NMC}}}{c_{s,max_0}^{\text{NMC}} V_{max}^{\text{NMC}}}$	
	$0 = \frac{\partial \epsilon_s^{\text{NMC}} c_s^{\text{NMC}}}{\partial t} - \nabla \cdot \left(D_{s,eff}^{\text{NMC}} \nabla \bar{c}_s^{\text{NMC}} \right) + \frac{a^{\text{NMC}} i^{\text{NMC}}}{F}$	
	$0 = \frac{\partial \varepsilon \bar{c}_e}{\partial t} - \nabla \cdot \left(D_{e,eff} \nabla \bar{c}_e \right) + \nabla \cdot \left(\bar{c}_e \left(-\frac{K^{\text{Cat}}}{\mu} \nabla \bar{p} \right) \right)$	
	$\quad - \nabla \left(\frac{t_+}{F} \cdot \kappa_{e,eff} \left(\nabla \bar{\varphi}_e - \frac{2(1-t_+)RT}{F} \frac{\nabla \bar{c}_e}{\bar{c}_e} \right) \right) - \frac{a^{\text{NMC}} i^{\text{NMC}}}{F}$	
	$0 = \nabla \cdot \left(-\kappa_{s,eff}^{\text{NMC}} \nabla \bar{\phi}_s^{\text{Cat}} \right) + a^{\text{NMC}} i^{\text{NMC}}$	
	$0 = \nabla \cdot \left(-\kappa_{e,eff} \nabla \bar{\varphi}_e + \frac{\kappa_{e,eff} 2(1-t_+)RT}{F} \frac{\nabla \bar{c}_e}{\bar{c}_e} \right) - a^{\text{NMC}} i^{\text{NMC}}$	
in Ω^{Sep}	$0 = \nabla \cdot \left(-\frac{K^{\text{Sep}}}{\mu} \nabla \bar{p} \right)$	$\bar{p} = p_D$ on Γ^{Out}
	$0 = \frac{\partial \varepsilon \bar{c}_e}{\partial t} - \nabla \cdot \left(D_{e,eff} \nabla \bar{c}_e \right) + \nabla \cdot \left(\bar{c}_e \left(-\frac{K^{\text{Sep}}}{\mu} \nabla \bar{p} \right) \right)$	
	$\quad - \nabla \left(\frac{t_+}{F} \cdot \kappa_{e,eff} \left(\nabla \bar{\varphi}_e - \frac{2(1-t_+)RT}{F} \frac{\nabla \bar{c}_e}{\bar{c}_e} \right) \right)$	
	$0 = \nabla \cdot \left(-\kappa_{e,eff} \nabla \bar{\varphi}_e + \frac{\kappa_{e,eff} 2(1-t_+)RT}{F} \frac{\nabla \bar{c}_e}{\bar{c}_e} \right)$	
in Ω^{Ano}	$0 = \nabla \cdot \left(-\frac{K^{\text{Ano}}}{\mu} \nabla \bar{p} \right) + \left(\frac{a^{\text{Si}} i^{\text{Si}}}{F} - \nabla \cdot \left(D_{s,eff}^{\text{Si}} \nabla \bar{c}_s^{\text{Si}} \right) \right) \hat{V}^{\text{Si}} \frac{V^{\text{Si}}}{c_{s,max_0}^{\text{Si}} V_{max}^{\text{Si}}}$	
	$\quad + \left(\frac{a^{\text{Gr}} i^{\text{Gr}}}{F} - \nabla \cdot \left(D_{s,eff}^{\text{Gr}} \nabla \bar{c}_s^{\text{Gr}} \right) \right) \hat{V}^{\text{Gr}} \frac{V^{\text{Gr}}}{c_{s,max_0}^{\text{Gr}} V_{max}^{\text{Gr}}}$	
	$0 = \frac{\partial \epsilon_s^{\text{Si}}}{\partial t} + \left(\frac{a^{\text{Si}} i^{\text{Si}}}{F} - \nabla \cdot \left(D_{s,eff}^{\text{Si}} \nabla \bar{c}_s^{\text{Si}} \right) \right) \hat{V}^{\text{Si}} \frac{V^{\text{Si}}}{c_{s,max_0}^{\text{Si}} V_{max}^{\text{Si}}}$	
	$0 = \frac{\partial \epsilon_s^{\text{Gr}}}{\partial t} + \left(\frac{a^{\text{Gr}} i^{\text{Gr}}}{F} - \nabla \cdot \left(D_{s,eff}^{\text{Gr}} \nabla \bar{c}_s^{\text{Gr}} \right) \right) \hat{V}^{\text{Gr}} \frac{V^{\text{Gr}}}{c_{s,max_0}^{\text{Gr}} V_{max}^{\text{Gr}}}$	
	$0 = \frac{\partial \epsilon_s^{\text{Si}} c_s^{\text{Si}}}{\partial t} - \nabla \cdot \left(D_{s,eff}^{\text{Si}} \nabla \bar{c}_s^{\text{Si}} \right) + \frac{a^{\text{Si}} i^{\text{Si}}}{F}$	
	$0 = \frac{\partial \epsilon_s^{\text{Gr}} c_s^{\text{Gr}}}{\partial t} - \nabla \cdot \left(D_{s,eff}^{\text{Gr}} \nabla \bar{c}_s^{\text{Gr}} \right) + \frac{a^{\text{Gr}} i^{\text{Gr}}}{F}$	
	$0 = \frac{\partial \varepsilon \bar{c}_e}{\partial t} - \nabla \cdot \left(D_{e,eff} \nabla \bar{c}_e \right) + \nabla \cdot \left(\bar{c}_e \left(-\frac{K^{\text{Ano}}}{\mu} \nabla \bar{p} \right) \right)$	
	$\quad - \nabla \left(\frac{t_+}{F} \cdot \kappa_{e,eff} \left(\nabla \bar{\varphi}_e - \frac{2(1-t_+)RT}{F} \frac{\nabla \bar{c}_e}{\bar{c}_e} \right) \right) - \frac{a^{\text{Si}} i^{\text{Si}} + a^{\text{Gr}} i^{\text{Gr}}}{F}$	
	$0 = \nabla \cdot \left(-\frac{\epsilon_s^{\text{Si}} \kappa_{s,eff}^{\text{Si}} + \epsilon_s^{\text{Gr}} \kappa_{s,eff}^{\text{Gr}}}{\epsilon_s^{\text{Si}} + \epsilon_s^{\text{Gr}}} \nabla \bar{\phi}_s^{\text{Ano}} \right) + a^{\text{Si}} i^{\text{Si}} + a^{\text{Gr}} i^{\text{Gr}}$	
	$0 = \nabla \cdot \left(-\kappa_{e,eff} \nabla \bar{\varphi}_e + \frac{\kappa_{e,eff} 2(1-t_+)RT}{F} \frac{\nabla \bar{c}_e}{\bar{c}_e} \right) - a^{\text{Si}} i^{\text{Si}} - a^{\text{Gr}} i^{\text{Gr}}$	
	$\bar{\phi}_s^{\text{Ano}} = 0$ on $\Gamma^{A\|CC}$	

and during electrolyte inflow as

$$N_k^{Li,\text{Free},in} = N_{k-1}^{Li,\text{Free}} + (t_k - t_{k-1}) \cdot \int_{\Gamma^{Out}} c_{e,k-1}^{\text{Free}} \left(-\frac{K}{\mu} \right) \nabla \bar{p} \cdot \boldsymbol{n} ds. \tag{29}$$

Hence, $c_e^{\text{Free}} = \frac{N_k^{Li,\text{Free},out/in}}{V_{e,k}^{\text{Free}}}$ is homogeneous in the whole reservoir. During discharging, Dirichlet boundary conditions are applied for the inflow of concentration, namely

$$\bar{c}_e = c_e^{\text{Free}} \quad \text{on } \Gamma^{Out}. \tag{30}$$

In addition to pressure driven convective flow also diffusive flow due to concentration differences in reservoir and electrode contribute to changes in electrolyte concentration, essentially during relaxation. Diffusional flow is captured by the Robin boundary condition

$$-D_{e,eff} \nabla \bar{c}_e \cdot \boldsymbol{n} = \frac{D_{e,eff}}{\delta} \left(\bar{c}_e - c_e^{\text{Free}} \right) \quad \text{on } \Gamma^{Out} \tag{31}$$

with the surface normal $\boldsymbol{n}$ and δ being the thickness of the boundary layer. This length value is approximated as the maximum reservoir thickness given by the initial electrolyte amount in the anode. Approximating the Péclet number

$$Pe = \frac{\delta \cdot \langle \boldsymbol{v} \rangle}{D_{e,eff}} \tag{32}$$

on Γ^{Out} indicates that convection and diffusion are of a similar magnitude for low C-rates, such that Eq. (31) is considered during charge

Table 2
Overview of the considered cells' properties with increasing anode Si fraction and Si-to-graphite ratio but constant capacity and initial porosity.

	Cell A	Cell B	Cell C	Cell D
Si Vol Frac within AM [%]	22.05	32.05	42.05	52.05
Anode Thickness [μm]	45	34.41	27.85	23.39
$\epsilon_{s,0}^{\mathrm{Si}}$ [–]	0.1142	0.1660	0.2178	0.2696
$\epsilon_{s,0}^{\mathrm{Gr}}$ [–]	0.4037	0.3519	0.3001	0.2483
K_0^{Ano} [m^2]	$6.6267 \cdot 10^{-14}$	$5.0546 \cdot 10^{-14}$	$3.6951 \cdot 10^{-14}$	$2.5481 \cdot 10^{-14}$
Electrolyte Amount [g/Ah]	2.2791	2.0769	1.9517	1.8665

and discharge as well (see Section S2.4). Hence,

$$N_k^{Li,\mathrm{Free}} = N_k^{Li,\mathrm{Free},out/in} + \left(t_k - t_{k-1}\right) \cdot \int_{\Gamma^{Out}} \frac{D_{e,eff}}{\delta} \left(\bar{c}_e - c_e^{\mathrm{Free}}\right) ds \quad (33)$$

completes the calculation of free electrolyte's Li concentration.

2.6. Simulation framework

The derived battery model is implemented in the open-source tool Firedrake, a finite element (FE) software using the UFL language in the python user interface [23,44–54]. Ai and Liu [55] provide latest insights into the advantages and disadvantages of the FE method in battery modeling alongside a list of open-source software. FE generally provides easy handling of challenging geometries and finite difference and finite volume offer a high resolution for discontinuous solutions. In this work, we employ a discontinuous Galerkin (DG) method which combines the mentioned advantages [56].

We use the `RectangleMesh` and `ExtrudedMesh` modules to obtain a hexahedral mesh of the 3D domain [57,58]. For the cylindrical cells, a discretization of $1 \cdot 10^{-6}$ m, $95 \cdot 10^{-3}$ m, and $0.35 \cdot 10^{-3}$ m in x-, y-, and z-direction, respectively, is applied. For the large format prismatic cell, on the other hand, the mesh sizes are set to $1 \cdot 10^{-6}$ m, $1 \cdot 10^{-2}$ m, and $1 \cdot 10^{-2}$ m in x-, y-, and z-direction, respectively, and height and width are adjusted accordingly. After introducing the DG function space of order 0, i.e. piecewise constant functions in each element, and defining the relevant subdomains, the derived DG weak formulation and a time stepping scheme are implemented [59]. The details are stated in Sections S1.3 and S1.4.

2.7. Simulation parameters

Simulations are performed for negative electrodes with different Si contents. The limiting case with 0 wt-% of Si serves as verification case and is presented in Section S2.1.

As reference case, we simulate the cell from our previous work [7] (cell A) with Si/graphite composite anode and NMC622 cathode. The anode has 20.8 wt-% nano-Si embedded in a carbon matrix. In our model, we use representative initial particle sizes of $R_{p_0}^{\mathrm{Si}} = 50$ nm and $R_{p_0}^{\mathrm{Gr}} = 4.89$ μm for Si and graphite, respectively. As electrolyte, we model 1 M $LiPF_6$ in ethylene carbonate (EC): diethylene carbonate (DEC) (3:7, wt). The electrolyte viscosity is $1.006 \cdot 10^{-3}$ Pa·s and it has a density of 1094 kg/m^3 [60]. Based on the microstructures of the electrodes used in our previous work, permeabilities are calculated to be $K^{\mathrm{Ano}} = 6.62665 \cdot 10^{-14}$ m^2 and $K^{\mathrm{Cat}} = 4.51344 \cdot 10^{-14}$ m^2 [61]. Hence, C^{Ano} and C^{Cat} are chosen accordingly. The applied parameter set is summarized in Table S1 and all simulations are isothermal at 298.15 K. The initial concentrations are set to match the initial potentials in [7]. Likewise, the maximum concentrations and electrode compositions result in an N/P ratio of 1.11 and the cell areal capacity is 29 Ah/m^2 (2.9 mAh/cm^2).

Furthermore, we consider cells with increasing Si fractions within the active material. As summarized in Table 2, the increasing Si fraction goes along with decreasing graphite fraction and anode thickness such that anode porosity and capacity remain constant.

3. Results and discussion

We start with the discussion of the results of the reference cell A, giving insights into the volume expansion induced electrolyte motion. First, we simulate a C/10 charge and discharge cycle including relaxation. Next, the effects of increasing C-rate and Si fraction are presented. Finally, we analyze the impact of different cell designs. The simulations contribute to the understanding of design aspects and their relevance for performance and degradation.

3.1. C/10 cycle of cell A

First, cell A is cycled in a voltage window between 3 and 4.3 V applying a constant current of C/10. After each charge or discharge the cell is relaxed for 1 h, meaning no current is applied. The (dis-)charging process is terminated when the respective voltage boundary is reached.

Fig. 2 (a) shows the course of cell voltage, anode and cathode potential during the charge, relaxation, discharge, and second relaxation. During the C/10 charge the cell voltage is comparable to the measurements in [7]. The discharge starts at 11 h after a rather short relaxation. The asymmetry between charge and discharge is observable in Fig. 2 (b). Here, the SOC of all three materials is depicted. It is calculated by averaging Equation (8) over the whole electrode domain. Similar to our previous work [7], we observe preferential lithiation of Si during charge. In the subsequent relaxation, the SOC of Si and NMC remain constant while the SOC of graphite increases slightly. A redistribution of Li from Si to graphite is observed. Still, the changed course of the graphite SOC during discharge compared to charge is clearly visible. Additionally, Fig. 2 (c) shows the volume fractions of the materials over time highlighting the major and significant expansion of Si particles. Consequently, electrolyte is displaced into the void regions of the cell as shown by Fig. 2 (d). Here, the electrolyte amount within and outside of Ω is depicted. The sum of those two volumes is constant, verifying the conservation of the incompressible liquid (see Section S2.3 for more discussion). The "breathing" of the cell is fully reversible over the course of one cycle which is in good agreement with the experimental results of Butler et al. [17].

Fig. 3 (a) shows the liquid phase pressure over time which also shows the lithiation competition of Si and graphite. During charge, the minimum values are at Γ^{Out} and the maximum values in the middle of the electrode in z-direction (see Figure S2 (b)). The 2D data in Fig. 3 (b) illustrates the velocity distribution at the end of charge. Si expansion induces electrolyte flow towards the reservoirs as indicated by the arrows. Moreover, the color legend indicates the magnitude of the flow. Electrolyte is displaced mainly in the anode and we see a flow through the separator towards the cathode. The magnitude of the velocity is comparable to [19]. Note that we observe outflow mostly through the cathode. This is opposite to observations in [20]. We will revisit this aspect in the discussions below. During relaxation the slight redistribution of Li causes minimal inflow. The inflow increases during discharge as anode material contracts (compare Figs. 3 (a) and (d)). Even more interesting than the amount of electrolyte is the Li concentration therein. Hence, the average concentrations in V_e^{Ω}, in one layer of discretization elements closest to the respective CCs, and in one layer of discretization elements closest to Γ^{Out} in the respective electrodes are

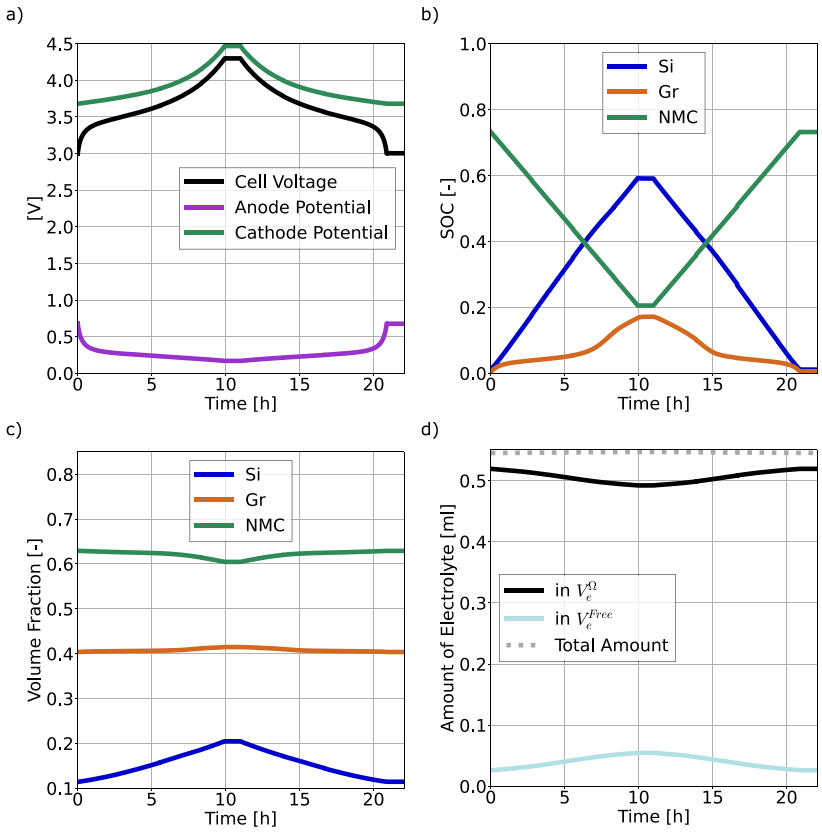

Fig. 2. Simulation results of C/10 full-cell charge, relaxation, discharge, and relaxation of cell A: Over time (a) the cell voltage, anode and cathode potential, (b) the average normalized Li concentration and (c) the volume fractions of the three active materials, and (d) the amount of electrolyte within and outside of Ω and the sum thereof are depicted.

calculated and plotted over time in Fig. 3 (c). The major concentration gradient occurs in x-direction such that the maximum and minimum values of $\bar{c}_e$ are at the cathode and the anode CCs, respectively, during charge and vice versa during discharge. Gradients over the height of the cell are negligible (see Figure S1 (a)). During discharge, no change in c_e^{Free} is expected as inflow does not impact c_e^{Free} and diffusion is minor along the whole outflow boundary. Still, slight deviations in the evolution of the concentration close to Γ^{Out} and the one at the CCs occur. Overall, the inflow of electrolyte with slightly increased concentration increases the concentration close to Γ^{Out}. Taking a close look at $\bar{c}_e$ close to Γ^{Out} during relaxation after discharge (> 21 h), one can see that there remains a concentration gradient in z-direction at the end of the simulation. See the Supplementary Material for details on relaxation after charging.

Solchenbach et al. [20] highlight the risk of Li plating in the anode close to Γ^{Out} due to a decreasing Li concentration in the electrolyte after several cycles. In the initial cycles studied in this work, the overpotential criteria is not met in our simulations even at higher C-rates. On the other hand, we want to point out the risk of oxygen evolution in the cathode if high degrees of delithiation are caused by major electrolyte motion through the cathode outflow boundary [62]. Hence, homogeneous electrolyte motion is desirable to avoid battery degradation.

3.2. Increasing Si fraction and C-rate

We simulate a C/3 discharge of fully relaxed cells immediately followed by a charge process with different C-rates ranging from C/10 to 2 C as concentration gradients are expected to be more prominent at higher C-rates. Omitting the rest time of 1 h compared to the slow cycling in the previous section suppresses equilibration processes resulting in a worst case scenario. Moreover, we consider cells A, B, C, and D as we analyze increasing Si fractions.

The effect of C-rate on the displaced electrolyte and the concentration therein is shown in Fig. 4 for the four different cells. By depicting c_e^{Free}, Fig. 4 (a) hints at the resulting concentration gradient within Ω which clearly increases with C-rate and Si fraction. A more detailed analysis of the equilibration of this gradient is conducted in Section S2.4. Fig. 4 (b) explains the increase of c_e^{Free} with C-rate and Si fraction. Increasing the applied current results in an increased concentration gradient in x-direction. Additionally, Fig. 4 (b) shows that with increasing Si content the flux through the cathode boundary increases, while the flux through the anode boundary actually decreases. Two effects contribute to this behavior. On the one hand, the effect of expansion on permeability is more pronounced at higher Si contents. This highlights that permeability is an important parameter affecting the concentration distribution. On the other hand, to keep the anode capacity constant, the increasing Si fraction goes along with decreasing anode thickness. Hence, the ratio of cathode outflow boundary size to the anode's one increases which allows for an increasing outflow through the cathode. This effect is enhanced by the decreasing anode permeability that goes along with increasing Si fraction. Due to the concentration gradient in x-direction, the increasing outflow through the cathode equals outflow of electrolyte with higher Li concentration. This effect is not observed for cells with constant anode thickness for increasing Si content and, hence, porosity and permeability. As outlined in Section S2.7, outflow occurs in those cases mainly through the anode. This emphasizes the relevance of electrode thickness and permeability ratio.

3.3. Effect of permeability

The permeability of porous media depends on the microstructure of the materials and can be tuned by the choice of materials or processing.

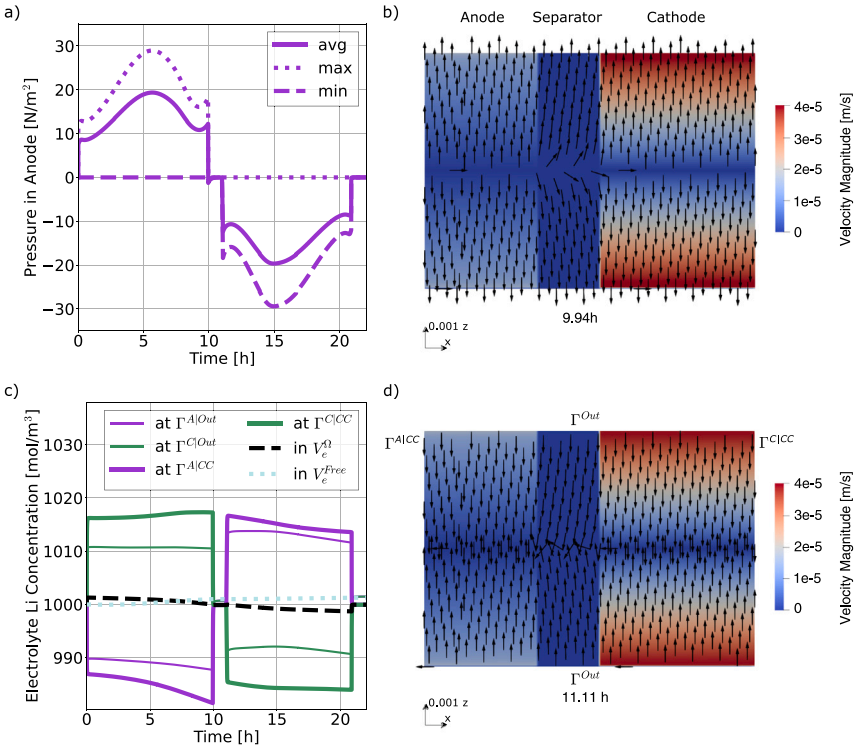

Fig. 3. Simulation results of C/10 full-cell charge, relaxation, discharge, and relaxation of cell A: Over time (a) the dynamic pressure within the anode and (c) the Li concentration in the electrolyte at varying regions within Ω and outside of Ω are depicted. Additionally, after (b) 9.94 h and (d) 11.11 h the 2D distribution of the velocity on the surface of Ω is shown. The color indicates the magnitude while the arrows indicate the direction. Additionally, descriptions of the boundaries are added.

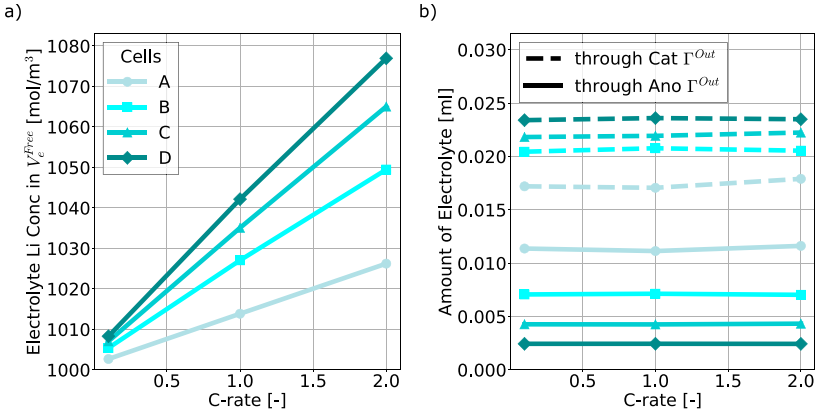

Fig. 4. Simulation results of C/10, 1 C, and 2 C charge of cells A, B, C, and D after 4.3 V is reached: (a) the Li concentration in the electrolyte outside of Ω and (b) the amount of electrolyte that left Ω either through the cathode or the anode are depicted.

Therefore, we vary the permeability in our simulations to investigate the effect on the concentration distribution. For cells A and D, we increase K^{Ano} to $K^{\text{Ano}} = 3 \cdot K^{\text{Cat}}$. To reach a three times higher permeability in the anode than in the cathode as in [20], $C^{\text{Ano}} = 180.34$ for cell A and $C^{\text{Ano}} = 69.35$ for cell D are determined. 2 C charge simulations are performed to analyze the impact. Additionally, we investigate the effect of improved separator permeability ($K^{\text{Sep}} = 10^{-16}$ m^2).

The results of the 2 C charge simulations of cells A and D with increased anode permeability, on the one hand, and with increased separator permeability, on the other hand, are shown in Fig. 5. Fig. 5 (a) presents the evolution of salt concentration in the free electrolyte volume. The two cells with increased K^{Sep} behave as we observed before, namely increasing c_e^{Free} above $\bar{c}_{e,0}$. In contrast, the higher K^{Ano} reduces c_e^{Free}. Hence, the plating risk increases [20]. Again, cell D reaches higher values than cell A. In order to explain the observations, the amount of electrolyte that flowed out through Γ^{Out} in the anode or cathode is plotted in Fig. 5 (b). Increased separator permeability favors electrolyte outflow through the cathode. In contrast, higher anode permeability in cell A favors electrolyte outflow through the anode, resulting in lower electrolyte concentrations in the reservoir which reproduces the results of Solchenbach et al. [20]. Interestingly, higher permeability in cell D initially also increases outflow through the anode with lower salt concentrations, however, after 0.15 h, anode permeability is reduced due to Si expansion and outflow through the cathode is favorable (see Fig. 5 (b)). As a result we observe a turning point in the evolution of reservoir concentration leading to a reservoir concentration close to initial conditions halfway through the charge.

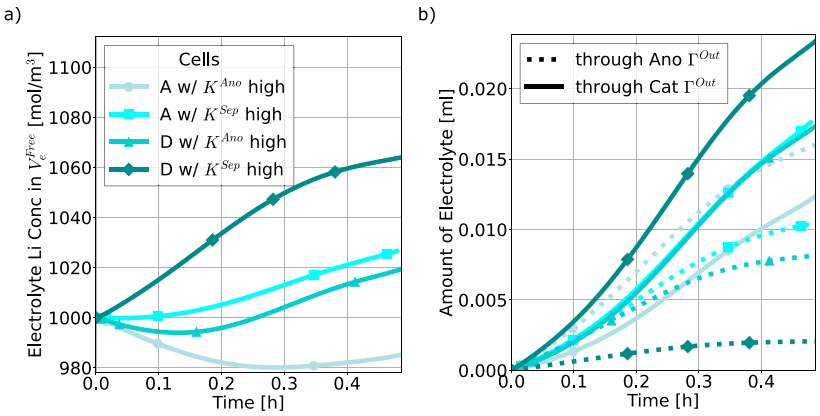

Fig. 5. Simulation results of 2 C full-cell charge of cells A and D with either increased anode or separator permeability: Over time (a) the Li concentration in the electrolyte outside of Ω and (b) the amount of electrolyte that flowed out either through the anode or the cathode boundaries are depicted.

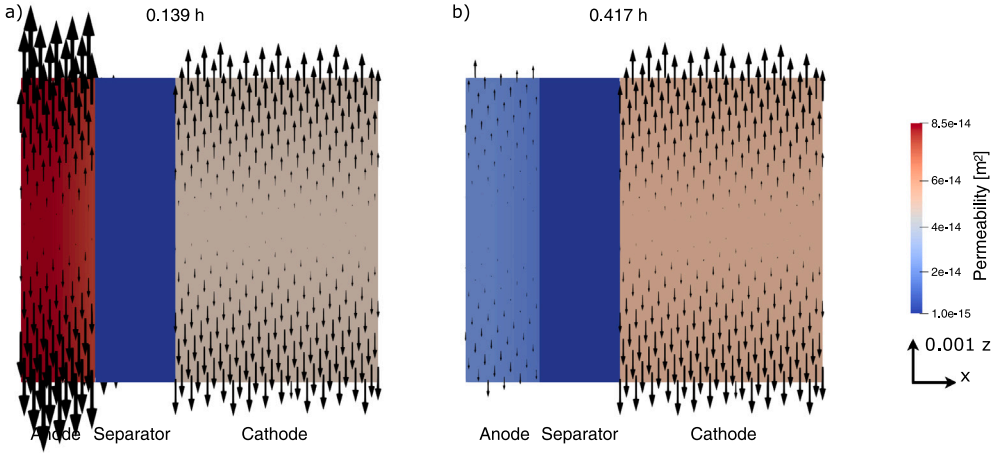

Fig. 6. Simulation results of 2 C full-cell charge of cell D with increased anode permeability: (a) After 0.139 h and (b) 0.417 h the permeability distribution indicated by color and the electrolyte flow velocity indicated by arrow length and direction are depicted. Separator permeability is constant at 10^{-17} m^2.

More details are given by Fig. 6 showing the permeability (color scale) and flow velocity (arrows) at two different points in time of the charge of cell D. Initially, the fastest electrolyte motion occurs in z-direction within the anode. Electrolyte motion in x-direction and within the separator is orders of magnitude smaller. As lithiation advances, the anode permeability decreases (see Fig. 6 (b)). Changes in cathode permeability are minor but converse such that we eventually observe a higher cathode permeability than anode permeability. Towards the end of charge electrolyte motion in the cathode dominates the outflow.

In conclusion, the adjusted composition of cell A with increased K^{Ano} leads to a depletion of Li in the free electrolyte reproducing the EMSI effect after prolonged cycling. At high Si contents in cell D, on the other hand, the evolution of the anode permeability leads to the change of outflow from anode to cathode reducing concentration differences between reservoir and electrode domain. This indicates that engineering the permeability of components is a pathway to reduce degradation effects. Note that degradation effects, especially the growth of solid electrolyte interphase (SEI) will also change the anode permeability. Especially, in combination with lithium plating we expect significant morphological changes which can also affect permeability and resulting electrolyte displacement. Additionally, concentrations of the conductive salt in the electrolyte allow for tuning of the cell performance. We find for example for cell D with higher K^{Ano} that the impact of transport parameters due to different salt concentrations does not significantly change the evolution of salt concentration in the free electrolyte volume. The absolute Li concentration difference between V_e^{Ω} and V_e^{Free} could be decreased by the utilization of a dilute electrolyte (see Section S2.8). Note that we did not use concentration dependent parameters. In case of fast charging or large concentration gradients, local transport properties could have a more pronounced effect.

3.4. Blade-type battery

Subsequently, the analysis of the large format prismatic cell with blade-type design is performed. We examine the composition of cell design A at 2 C charge. Characteristic for the blade design is the increased height-to-length ratio (z/x = 90.3 cm/133 μm). Therefore, higher pressure gradients and, thus, velocities are expected. This goes along with a higher total amount of electrolyte. Additionally, we investigate two outflow scenarios representing stacked and wound up cells. This also highlights the capability of the 3D model.

Fig. 7 summarizes simulation results of the two cell types. Our simulations predict no significant changes in concentration distributions between the two approaches. Moreover, the final concentration in V_e^{Free} is similar compared to the results for cylindrical cells shown in Fig. 4 (a). Therefore, electrode thickness and permeability ratios are regarded as relevant parameters determining the concentration in V_e^{Free}. In contrast, the influence on the pressure distribution is significant, as shown in Figs. 4 (b) and (c). The pressure level reduces by two orders of

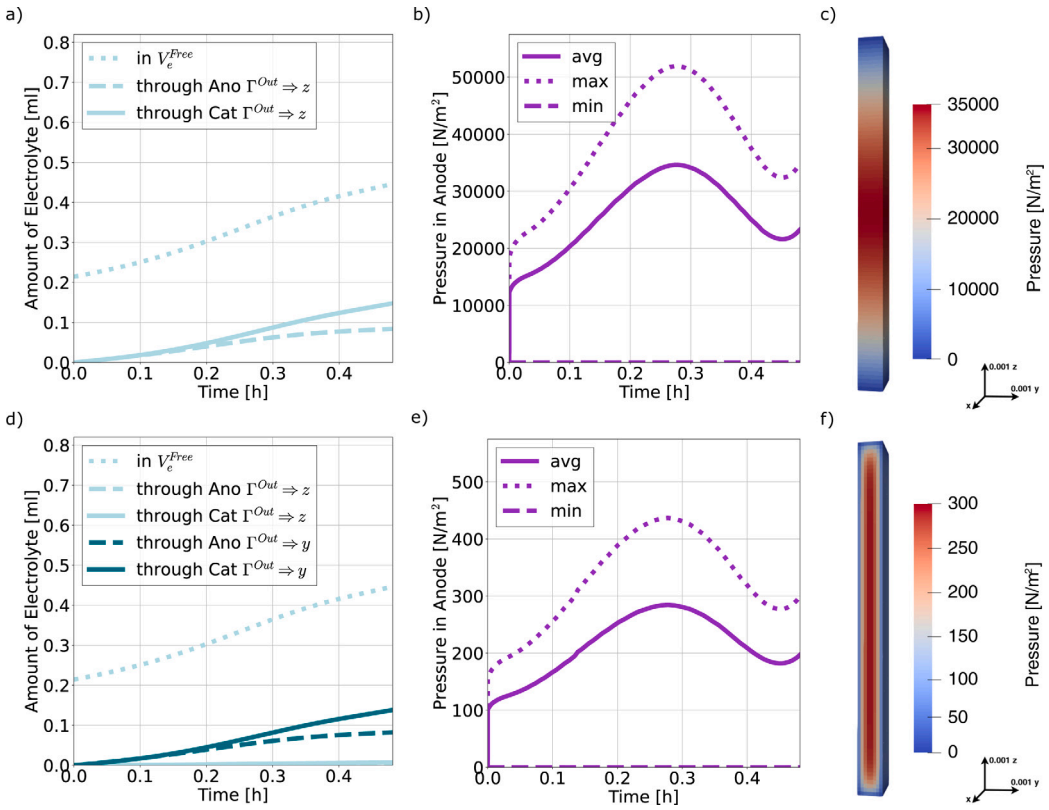

Fig. 7. Simulation results of 2 C full-cell charge of blade-type prismatic cell with cell design A: Over time the amount of electrolyte that flowed out through the varying boundaries and the pressure in the anode for (a) and (b) outflow in z-direction (wound up prismatic cell) and (d) and (e) outflow in y- and z-direction (stacked prismatic cell) are depicted, respectively. Likewise for both outflow scenario, (c) and (f) show the 3D pressure distribution at the end of lithiation, respectively.

magnitude in a cell design enabling outflow in y-direction (see Figs. 4 (e) and (f)). Thus, in a stacked prismatic cell less stress is expected than in a wound up prismatic cell.

The authors would like to add that p_D does not need to be constant. Applying a function in space and time allows the analysis of further outflow scenario resembling for example limited electrolyte reservoirs.

4. Conclusions

This research paper introduces a homogenized 3D battery model that includes active material particle expansion and contraction in order to study the induced electrolyte motion. In the volume-averaged domain, anode, separator, and cathode consisting of solid and liquid material are modeled. Within the electrodes, active material particles are assumed to expand and contract upon lithiation and delithiation pushing the incompressible electrolyte out of the domain or soaking it back in. Hence, the focus of this study is not only on the electrolyte Li concentration within the domain but also outside of it.

Simulating the C/10 charge and discharge of a Si/graphite-NMC622 full-cell allows us to determine first electrochemical trends like concentration gradients in through direction and flow direction. Relaxation simulations showcase that several days of rest time are necessary to equilibrate the cell and potentially avoid accumulation of inhomogeneities over cycling. The study of varying Si contents, C-rates, and permeabilities analyzes the gap between the Li concentration in the electrolyte within and outside of the domain. Crucial factors like anode thickness and permeability that govern the Li concentration in the free electrolyte are identified. Finally, cells with even higher length-scales and varying outflow boundaries are considered. This contributes to the understanding of electrolyte flow and its effects.

Our simulations highlight that differences in permeability of components favor inhomogeneities in salt concentration between the cell domain and the free volume. Tuning the permeability of components provides a strategy to mitigate degradation mechanisms originating from this effect. Structuring techniques such as multi-layer coating or perforation allow to specifically adjust the permeability of the electrodes and provide additional benefits for ultra-fast charging [63]. Moreover, we emphasize that degradation phenomena are extremely complicated and a myriad of coupled processes contribute to the failure of the cell. SEI growth, electrolyte dry-out, Li plating, loss of active material, and particle cracking due to mechanical stress have to be considered to provide a comprehensive description of capacity fade and prediction of cycle life [64]. While this is beyond the scope of this work, we implement our model in an open-source simulation tool providing a framework for the community for future developments.

CRediT authorship contribution statement

Lioba Boveleth: Writing – original draft, Visualization, Software, Methodology, Investigation, Conceptualization. **Max Okraschevski:** Writing – review & editing, Software, Methodology. **Timo Danner:** Writing – review & editing, Supervision, Conceptualization. **Arnulf Latz:** Writing – review & editing, Funding acquisition.

Declaration of competing interest

The authors declare that they have no known competing financial interests or personal relationships that could have appeared to influence the work reported in this paper.

Acknowledgments

The authors would like to thank the German Federal Ministry of Education and Research (BMBF) for the funding of the project CharLiSiKo (03XP0333C) managed by Projektträger Jülich (PTJ). The work performed at DLR contributes to the research at CELEST (Center for Electrochemical Energy Storage Ulm-Karlsruhe).

Appendix A. List of symbols

0	Initial value
A_{cell}	Cell surface area
a	Specific surface area
C	Carman–Kozeny constant
c	Li concentration
D	Diffusion constant
e	Electrolyte
F	Faraday constant [96485.332 C/mol]
J	Source term for Li
j	Li flux
K	Permeability
k	Iteration steps over time
I_{app}	Applied current
i	Current density
mat	Material Si, graphite or NMC622
max	Maximum value
N^{Li}	Amount of Li
Pe	Péclet number
P	Absolute pressure
p	Dynamic pressure
R	Ideal gas constant [8.3144621 J/(mol K)]
R_p	Particle radius
Re	Reynolds number
s	Solid
Sc	Schmidt number
T	Temperature [298.15 K]
t	Time
t_+	Transference number
V	Molar volume
$\mathcal{V}$	Averaging volume
$\boldsymbol{v}$	Velocity
x	Normalized Li concentration
Γ	Simulation domain boundary
δ	Characteristic length of diffusion
ε	Porosity
ε_s	Volume fraction
ζ	Dummy variable
κ_s	Electronic conductivity
κ_e	Ionic conductivity
μ	Dynamic viscosity
ν	Kinematic viscosity
ρ	Density
τ	Tortuosity
ϕ_s	Electric potential
φ_e	Electrochemical potential
Ω	Simulation domain

Appendix B. Supplementary data

Supplementary material related to this article can be found online at https://doi.org/10.1016/j.est.2025.119206.

Data availability

Data will be made available on request.

References

[1] R. Chandrasekaran, A. Magasinski, G. Yushin, T.F. Fuller, Analysis of lithium insertion/deinsertion in a silicon electrode particle at room temperature, J. Electrochem. Soc. 157 (10) (2010) A1139, http://dx.doi.org/10.1149/1.3474225.

[2] Z. Chen, L. Christensen, J. Dahn, Large-volume-change electrodes for li-ion batteries of amorphous alloy particles held by elastomeric tethers, Electrochem. Commun. 5 (11) (2003) 919–923, http://dx.doi.org/10.1016/j.elecom.2003.08.017.

[3] W. Yu, P. Li, X. Zhang, D. Ma, H. Huang, H. Zhang, Does the electrolyte flow in a lithium-ion battery? A perspective from the electrochemical–thermal–hydraulic–mechanical coupling in porous media, Phys. Fluids 35 (11) (2023) 113103, http://dx.doi.org/10.1063/5.0172492.

[4] S. Chae, S.-H. Choi, N. Kim, J. Sung, J. Cho, Integration of graphite and silicon anodes for the commercialization of high-energy lithium-ion batteries, Angew. Chem. Int. Ed. 59 (1) (2020) 110–135, http://dx.doi.org/10.1002/anie.201902085.

[5] P. Li, H. Kim, S.-T. Myung, Y.-K. Sun, Diverting exploration of silicon anode into practical way: A review focused on silicon-graphite composite for lithium ion batteries, Energy Storage Mater. 35 (2021) 550–576, http://dx.doi.org/10.1016/j.ensm.2020.11.028.

[6] D. Vidal, C. Leys, B. Mathieu, N. Guillet, V. Vidal, D. Borschneck, P. Chaurand, S. Genies, E. De Vito, M. Tulodziecki, W. Porcher, Si–c/g based anode swelling and porosity evolution in 18650 casing and in pouch cell, J. Power Sources 514 (2021) 230552, http://dx.doi.org/10.1016/j.jpowsour.2021.230552.

[7] C. Hogrefe, N. Paul, L. Boveleth, M. Bolsinger, M. Flügel, T. Danner, A. Latz, R. Gilles, V. Knoblauch, M. Wohlfahrt-Mehrens, M. Hölzle, T. Waldmann, Lithium redistribution mechanism within silicon-graphite electrodes: Multi-method approach and method validation, J. Electrochem. Soc. 171 (2024) 070503, http://dx.doi.org/10.1149/1945-7111/ad59c7.

[8] L. Boveleth, A. Lindner, W. Menesklou, T. Danner, A. Latz, Material parameters affecting li plating in si/graphite composite electrodes, Electrochim. Acta 506 (2024) 145010, http://dx.doi.org/10.1016/j.electacta.2024.145010.

[9] M. Flügel, M. Bolsinger, M. Marinaro, V. Knoblauch, M. Hölzle, M. Wohlfahrt-Mehrens, T. Waldmann, Onset shift of li plating on si/graphite anodes with increasing si content, J. Electrochem. Soc. 170 (6) (2023) 060536, http://dx.doi.org/10.1149/1945-7111/acdda3.

[10] J. Müller, P. Michalowski, A. Kwade, Impact of silicon content and particle size in lithium-ion battery anodes on particulate properties and electrochemical performance, Batteries 9 (7) (2023) http://dx.doi.org/10.3390/batteries9070377.

[11] Z. Yang, S.E. Trask, X. Wu, B.J. Ingram, Effect of si content on extreme fast charging behavior in silicon–graphite composite anodes, Batteries 9 (2) (2023) http://dx.doi.org/10.3390/batteries9020138.

[12] W. Mai, A. Colclasure, K. Smith, A reformulation of the pseudo2d battery model coupling large electrochemical–mechanical deformations at particle and electrode levels, J. Electrochem. Soc. 166 (8) (2019) A1330, http://dx.doi.org/10.1149/2.0101908jes.

[13] M. Ge, C. Cao, G.M. Biesold, C.D. Sewell, S.-M. Hao, J. Huang, W. Zhang, Y. Lai, Z. Lin, Recent advances in silicon-based electrodes: From fundamental research toward practical applications, Adv. Mater. 33 (16) (2021) 2004577, http://dx.doi.org/10.1002/adma.202004577.

[14] L. von Kolzenberg, A. Latz, B. Horstmann, Chemo-mechanical model of sei growth on silicon electrode particles, Batter. Supercaps 5 (2) (2022) e202100216, http://dx.doi.org/10.1002/batt.202100216.

[15] X. Li, Z. Zhang, L. Gong, K. Fu, H. Yang, C. Wang, P. Tan, Modelling and analysis of the volume change behaviors of li-ion batteries with silicon-graphene composite electrodes, Chem. Eng. J. 470 (2023) 144188, http://dx.doi.org/10.1016/j.cej.2023.144188.

[16] C.P. Aiken, N. Kowalski, R.C. Fitzner, S. Trussler, J.E. Harlow, E.J. Butler, J.R. Dahn, Tracking electrolyte motion in cylindrical li-ion cells using moment of inertia measurements, J. Electrochem. Soc. 170 (4) (2023) 040529, http://dx.doi.org/10.1149/1945-7111/acce72.

[17] E.J. Butler, N. Kowalski, J. Jager, M.B. Johnson, J.E. Harlow, M. Metzger, J.R. Dahn, Quantifying electrolyte motion in cylindrical li-ion cells using rotational inertia measurements, J. Electrochem. Soc. 172 (6) (2025) 060526, http://dx.doi.org/10.1149/1945-7111/ade010.

[18] T. Bond, S. Gasilov, R. Dressler, R. Petibon, S. Hy, J.R. Dahn, Operando 3d imaging of electrolyte motion in cylindrical li-ion cells, J. Electrochem. Soc. 172 (3) (2025) 030512, http://dx.doi.org/10.1149/1945-7111/adba8f.

[19] S. Kulathu, J.A. Hurtado, K. Bose, Y. Hahn, P.A. Bouzinov, R.L. Taylor, V. Oancea, A three-dimensional thermal-electrochemical–mechanical-porous flow multiscale formulation for battery cells, Internat. J. Numer. Methods Engrg. 125 (13) (2024) e7464, http://dx.doi.org/10.1002/nme.7464.

[20] S. Solchenbach, C. Tacconis, A. Gomez Martin, V. Peters, L. Wallisch, A. Stanke, J. Hofer, D. Renz, B. Lewerich, G. Bauer, M. Wichmann, D. Goldbach, A. Adam, M. Spielbauer, P. Lamp, J. Wandt, Electrolyte motion induced salt inhomogeneity – a novel aging mechanism in large-format lithium-ion cells, Energy Env. Sci. 17 (2024) 7294–7317, http://dx.doi.org/10.1039/D4EE03211J.

[21] A.-S. Hamedi, E.M. Shumway, D.R. Wheeler, Electrode-level modeling of silicon anodes for improved cell design, J. Electrochem. Soc. 171 (12) (2024) 120539, http://dx.doi.org/10.1149/1945-7111/ad9fe4.

[22] T. Waldmann, C. Hogrefe, M. Flügel, I. Pivarníková, C. Weisenberger, E. Delz, M. Bolsinger, L. Boveleth, N. Paul, M. Kasper, M. Feinauer, R. Schäfer, K. Bischof, T. Danner, V. Knoblauch, P. Müller-Buschbaum, R. Gilles, A. Latz, M. Hölzle, M. Wohlfahrt-Mehrens, Efficient workflows for detecting li depositions in lithium-ion batteries, J. Electrochem. Soc. 171 (7) (2024) 070526, http://dx.doi.org/10.1149/1945-7111/ad5ef8.

[23] D.A. Ham, P.H.J. Kelly, L. Mitchell, C.J. Cotter, R.C. Kirby, K. Sagiyama, N. Bouziani, S. Vorderwuelbecke, T.J. Gregory, J. Betteridge, D.R. Shapero, R.W. Nixon-Hill, C.J. Ward, P.E. Farrell, P.D. Brubeck, I. Marsden, T.H. Gibson, M. Homolya, T. Sun, A.T.T. McRae, F. Luporini, A. Gregory, M. Lange, S.W. Funke, F. Rathgeber, G.-T. Bercea, G.R. Markall, Firedrake User Manual, first ed., Imperial College London and University of Oxford and Baylor University and University of Washington, 2023, http://dx.doi.org/10.25561/104839.

[24] S. Hasan, s. M. A. Bashar, A.A.N. Tamzid, R. Hossain, M. Haque, M. Rahaman, Can the future of electric vehicles be changed by byd blade battery?-a short review, 2023.

[25] R.B. Hossain, S.M.N. Sakib, M.F. Rabbi, S. Islam, P. Roy, S. Hasan, A comprehensive review of blade battery technology for the vehicle industry, 2023, http://dx.doi.org/10.5281/zenodo.8049205.

[26] F. Chen, W. Zhu, X. Kong, Y. Huang, Y. Wang, Y. Zheng, D. Ren, Study on the homogeneity of large-size blade lithium-ion batteries based on thermoelectric coupling model simulation, Energies 15 (24) (2022) 00, http://dx.doi.org/10.3390/en15249556.

[27] S. Whitaker, The Method of Volume Averaging, Springer Dordrecht, 1999, http://dx.doi.org/10.1007/978-94-017-3389-2.

[28] T. Schmitt, A. Latz, B. Horstmann, 1999Ed model and a stable numerical algorithm for multi-dimensional simulations of conversion batteries, Electrochim. Acta 333 (2020) 135491, http://dx.doi.org/10.1016/j.electacta.2019.135491.

[29] T.I. Evans, T.V. Nguyen, R.E. White, A mathematical model of a lithium/thionyl chloride primary cell, J. Electrochem. Soc. 136 (2) (1989) 328, http://dx.doi.org/10.1149/1.2096630.

[30] F.H. Bark, F. Alavyoon, Convection in electrochemical systems, Appl. Sci. Res. 53 (1994) 11–34, http://dx.doi.org/10.1007/BF00849647.

[31] A. Latz, J. Zausch, Thermodynamic consistent transport theory of li-ion batteries, J. Power Sources 196 (6) (2011) 3296–3302, http://dx.doi.org/10.1016/j.jpowsour.2010.11.088.

[32] G.W. Richardson, J.M. Foster, R. Ranom, C.P. Please, A.M. Ramos, Charge transport modelling of lithium-ion batteries, European J. Appl. Math. 33 (6) (2022) 983–1031, http://dx.doi.org/10.1017/S0956792521000292.

[33] D.J. Pereira, A.M. Aleman, J.W. Weidner, T.R. Garrick, A mechano-electrochemical battery model that accounts for preferential lithiation inside blended silicon graphite (si/c) anodes, J. Electrochem. Soc. 169 (2) (2022) 020577, http://dx.doi.org/10.1149/1945-7111/ac554f.

[34] M.N. Obrovac, L. Christensen, D.B. Le, J.R. Dahn, Alloy design for lithium-ion battery anodes, J. Electrochem. Soc. 154 (9) (2007) A849, http://dx.doi.org/10.1149/1.2752985.

[35] R. Chandrasekaran, T.F. Fuller, Analysis of the lithium-ion insertion silicon composite electrode/separator/lithium foil cell, J. Electrochem. Soc. 158 (8) (2011) A859, http://dx.doi.org/10.1149/1.3589301.

[36] A.J. Louli, J. Li, S. Trussler, C.R. Fell, J.R. Dahn, Volume, Pressure and thickness evolution of li-ion pouch cells with silicon-composite negative electrodes, J. Electrochem. Soc. 164 (12) (2017) A2689, http://dx.doi.org/10.1149/2.1691712.

[37] R. Koerver, W. Zhang, L. de Biasi, S. Schweidler, A.O. Kondrakov, S. Kolling, T. Brezesinski, P. Hartmann, W.G. Zeier, J. Janek, Chemo-mechanical expansion of lithium electrode materials – on the route to mechanically optimized all-solid-state batteries, Energy Env. Sci. 11 (2018) 2142–2158, http://dx.doi.org/10.1039/C8EE00907D.

[38] Plotdigitizer: Version 3.1.6, 2024, https://plotdigitizer.com.

[39] T.M. Inc., [Matlab version: 9.7.0.1216025 (r2019b)], 2019, https://www.mathworks.com.

[40] F. Durst, Grundlagen der Strömungsmechanik, Springer Berlin, Heidelberg, 2006, http://dx.doi.org/10.1007/978-3-540-31324-3.

[41] F.J. Valdes-Parada, J.A. Ochoa-Tapia, J. Alvarez-Ramirez, Validity of the permeability Carman–Kozeny equation: A volume averaging approach, Phys. A 388 (6) (2009) 789–798, http://dx.doi.org/10.1016/j.physa.2008.11.024.

[42] S.S. Zhang, A review on the separators of liquid electrolyte li-ion batteries, J. Power Sources 164 (1) (2007) 351–364, http://dx.doi.org/10.1016/j.jpowsour.2006.10.065.

[43] B. Yuan, K. Wen, D. Chen, Y. Liu, Y. Dong, C. Feng, Y. Han, J. Han, Y. Zhang, C. Xia, A. (Xueliang) Sun, W. He, Composite separators for robust high rate lithium ion batteries, Adv. Funct. Mater. 31 (32) (2021) 2101420, http://dx.doi.org/10.1002/adfm.202101420.

[44] S. Balay, S. Abhyankar, M.F. Adams, S. Benson, J. Brown, P. Brune, K. Buschelman, E. Constantinescu, L. Dalcin, A. Dener, V. Eijkhout, J. Faibussowitsch, W.D. Gropp, V. Hapla, T. Isaac, P. Jolivet, D. Karpeev, D. Kaushik, M.G. Knepley, F. Kong, S. Kruger, D.A. May, L.C. McInnes, R.T. Mills, L. Mitchell, T. Munson, J.E. Roman, K. Rupp, P. Sanan, J. Sarich, B.F. Smith, S. Zampini, H. Zhang, H. Zhang, J. Zhang, PETSc/TAO Users Manual, Tech. Rep. ANL-21/39, Argonne National Laboratory, 2024, http://dx.doi.org/10.2172/2205494, Revision 3.21.

[45] S. Balay, W.D. Gropp, L.C. McInnes, B.F. Smith, Efficient management of parallelism in object oriented numerical software libraries, in: E. Arge, A.M. Bruaset, H.P. Langtangen (Eds.), Modern Software Tools in Scientific Computing, Birkhäuser Press, 1997, pp. 163–202.

[46] L.D. Dalcin, R.R. Paz, P.A. Kler, A. Cosimo, Parallel distributed computing using python, Adv. Water Resour. 34 (9) (2011) 1124–1139, http://dx.doi.org/10.1016/j.advwatres.2011.04.013, new Computational Methods and Software Tools.

[47] M. Lange, L. Mitchell, M.G. Knepley, G.J. Gorman, Efficient mesh management in Firedrake using PETSc-DMPlex, SIAM J. Sci. Comput. 38 (5) (2016) S143–S155, http://dx.doi.org/10.1137/15M1026092, arXiv:http://arxiv.org/abs/1506.07749.

[48] M. Homolya, D.A. Ham, A parallel edge orientation algorithm for quadrilateral meshes, SIAM J. Sci. Comput. 38 (5) (2016) S48–S61, http://dx.doi.org/10.1137/15M1021325, http://arxiv.org/abs/1505.03357. [arXiv:1505.03357].

[49] A.T.T. McRae, G.-T. Bercea, L. Mitchell, D.A. Ham, C.J. Cotter, Automated generation and symbolic manipulation of tensor product finite elements, SIAM J. Sci. Comput. 38 (5) (2016) S25–S47, http://dx.doi.org/10.1137/15M1021167, arXiv:1411.2940.

[50] G. Bercea, A.T.T. McRae, D.A. Ham, L. Mitchell, F. Rathgeber, L. Nardi, F. Luporini, P.H.J. Kelly, A structure-exploiting numbering algorithm for finite elements on extruded meshes, and its performance evaluation in firedrake, Geosci. Model. Dev. 9 (10) (2016) 3803–3815, http://dx.doi.org/10.5194/gmd-9-3803-2016, arXiv:1604.05937.

[51] Lawrence Livermore National Laboratory, *hypre*: High Performance Preconditioners. https://www.llnl.gov/casc/hypre.

[52] F. Luporini, D.A. Ham, P.H.J. Kelly, An algorithm for the optimization of finite element integration loops, ACM Trans. Math. Software 44 (2017) 3:1–3:26, http://dx.doi.org/10.1145/3054944, arXiv:1604.05872.

[53] M. Homolya, L. Mitchell, F. Luporini, D.A. Ham, TSFC: a structure-preserving form compiler, 2017, arXiv:1705.03667. http://arxiv.org/abs/1705.003667.

[54] M. Homolya, R.C. Kirby, D.A. Ham, Exposing and exploiting structure: optimal code generation for high-order finite element methods, 2017, arXiv:1711.02473. http://arxiv.org/abs/1711.02473.

[55] W. Ai, Y. Liu, Jubat, A julia-based framework for battery modelling using finite element method, SoftwareX 27 (2024) http://dx.doi.org/10.1016/j.softx.2024.101760.

[56] M. Zhang, C.-W. Shu, An analysis of and a comparison between the discontinuous galerkin and the spectral finite volume methods, Comput. & Fluids 34 (4) (2005) 581–592, http://dx.doi.org/10.1016/j.compfluid.2003.05.006.

[57] G.-T. Bercea, A.T.T. McRae, D.A. Ham, L. Mitchell, F. Rathgeber, L. Nardi, F. Luporini, P.H.J. Kelly, A structure-exploiting numbering algorithm for finite elements on extruded meshes, and its performance evaluation in firedrake, Geosci. Model. Dev. 9 (10) (2016) 3803–3815, http://dx.doi.org/10.5194/gmd-9-3803-2016.

[58] A.T.T. McRae, G.-T. Bercea, L. Mitchell, D.A. Ham, C.J. Cotter, Automated generation and symbolic manipulation of tensor product finite elements, SIAM J. Sci. Comput. 38 (5) (2016) S25–S47, http://dx.doi.org/10.1137/15M1021167.

[59] T. Roy, T.B. Jönsthövel, C. Lemon, A.J. Wathen, A block preconditioner for non-isothermal flow in porous media, J. Comput. Phys. 395 (2019) 636–652, http://dx.doi.org/10.1016/j.jcp.2019.06.038.

[60] S. Uchida, T. Kiyobayashi, What differentiates the transport properties of lithium electrolyte in ethylene carbonate mixed with diethylcarbonate from those mixed with dimethylcarbonate? J. Power Sources 511 (2021) 230423, http://dx.doi.org/10.1016/j.jpowsour.2021.230423.

[61] M. GmbH, Geodict simulation software release, 2023, http://dx.doi.org/10.30423/release.geodict2023.

[62] R. Jung, M. Metzger, F. Maglia, C. Stinner, H.A. Gasteiger, Oxygen release and its effect on the cycling stability of $LiNi_xMn_yCo_zO_2$ (nmc) cathode materials for li-ion batteries, J. Electrochem. Soc. 164 (7) (2017) A1361, http://dx.doi.org/10.1149/2.0021707jes.

[63] M. Clausnitzer, T. Danner, B. Prifling, M. Neumann, V. Schmidt, A. Latz, Influence of electrode structuring techniques on the performance of all-solid-state batteries, Batter. Supercaps 7 (4) (2024) http://dx.doi.org/10.1002/batt.202300522, e202300522.

[64] R. Li, N.D. Kirkaldy, F.F. Oehler, M. Marinescu, G.J. Offer, S.E.J. O'Kane, The importance of degradation mode analysis in parameterising lifetime prediction models of lithium-ion battery degradation, Nat. Commun. 16 (1) (2025) 2776, http://dx.doi.org/10.1038/s41467-025-57968-3.